JOURNAL OF SYNCHROTRON RADIATION
ISSN 1600-5775

A comparison of parametric and integrative approaches for X-ray fluorescence analysis applied to a Stroke model

Andrew M. Crawford,[a]* Nicole J. Sylvain,[b] Huishu Hou,[b] Mark J. Hackett,[c,d] M. Jake Pushie,[b] Ingrid J. Pickering,[a] Graham N. George[a] and Michael E. Kelly[b]

[a]Geology, University of Saskatchewan, 114 Science Place, Saskatoon, Saskatchewan S7N 5E2, Canada, [b]Division of Neurosurgery, Department of Surgery, College of Medicine, University of Saskatchewan, 103 Hospital Drive, Saskatoon, Saskatchewan S7N 0W8, Canada, [c]Curtin Institute for Functional Molecules and Interfaces, Department of Chemistry, Faculty of Science and Engineering, Curtin University, Kent Street, Bently, Western Australia 6102, Australia, and [d]Curtin Health Innovation Research Institute, Curtin University, Kent Street, Bently, Western Australia 6102, Australia. *Correspondence e-mail: andrew.crawford@usask.ca

Received 10 April 2018
Accepted 29 July 2018

Edited by R. W. Strange, University of Essex, UK

Keywords: *M-BLANK*; X-ray fluorescence; strokes; window binning; Xpress 3 electronics.

Synchrotron X-ray fluorescence imaging enables visualization and quantification of microscopic distributions of elements. This versatile technique has matured to the point where it is used in a wide range of research fields. The method can be used to quantitate the levels of different elements in the image on a pixel-by-pixel basis. Two approaches to X-ray fluorescence image analysis are commonly used, namely, (i) integrative analysis, or window binning, which simply sums the numbers of all photons detected within a specific energy region of interest; and (ii) parametric analysis, or fitting, in which emission spectra are represented by the sum of parameters representing a series of peaks and other contributing factors. This paper presents a quantitative comparison between these two methods of image analysis using X-ray fluorescence imaging of mouse brain-tissue sections; it is shown that substantial errors can result when data from overlapping emission lines are binned rather than fitted. These differences are explored using two different digital signal processing data-acquisition systems with different count-rate and emission-line resolution characteristics. Irrespective of the digital signal processing electronics, there are substantial differences in quantitation between the two approaches. Binning analyses are thus shown to contain significant errors that not only distort the data but in some cases result in complete reversal of trends between different tissue regions.

1. Introduction

Cells, tissues and organs all contain a variety of bulk, trace and ultra-trace elements – the metallome – in addition to organic constituents. In most cases, interconnected homeostatic mechanisms maintain these elemental concentrations, often within narrow limits. Relevant concentrations range from 10–100 m*M* for bulk elements (*e.g.* P, K, Na and Fe in red blood cells) to 100 µ*M*–3 m*M* for trace elements (*e.g.* Zn, Mg, Ca and Fe in other cell types) to 1–20 µ*M* for ultra-trace elements (*e.g.* Cu, Ni, Mn and Se in blood) (Herring *et al.*, 1960*a*; Shamberger, 2003). These concentrations are perturbed under various conditions and disease states (Herring *et al.*, 1960*b*; Kakkar & Makkar, 2009), and these variations can be clinically diagnostic.

There are several methods that can sufficiently measure cellular- and tissue-specific elemental compositions; these include mass spectrometry (MS), metal-specific organic fluorophores and intrinsic X-ray fluorescence (XRF) (Penner-

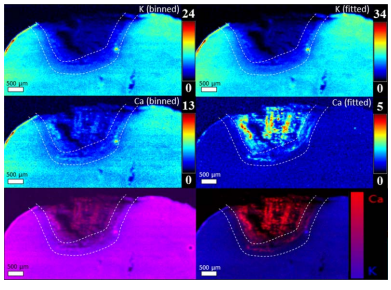

Hahn, 2014; McRae *et al.*, 2009; Pushie *et al.*, 2014). Fluorescent probes have informed studies on the subcellular transition metal cations Zn (Fierke & Thompson, 2001; Wang *et al.*, 2012; Kikuchi *et al.*, 2004) and Cu (Yang *et al.*, 2005) as well as others, and can have excellent sensitivity. Unfortunately, in order for fluorescent probes to function they must interact with the metal of interest, meaning they only detect the labile (free) metal ions, and also have problems detecting paramagnetic ions as a result of intersystem crossing (Penner-Hahn, 2014). Moreover, since fluorescent probes must bind the metals to report on metal content, this can disrupt metal homeostasis and all competitive binding equilibria must be taken into account to accurately calculate the total biological content. MS methods can have great to exquisite sensitivity. For example, multi-element detection using inductively coupled plasma MS (Miyashita *et al.*, 2014; Mueller *et al.*, 2014; Ho & Chan, 2010) or quadrupole MS detection (Groombridge *et al.*, 2013) can detect as few as 10^5 atoms per cell, whereas time-of-flight MS has weaker sensitivity. Unfortunately, MS methods for cell/tissue analysis can be challenging owing to incomplete vaporization/ionization, the need for vacuum conditions and variable ionization efficiencies for different elements caused by matrix effects.

In contrast to these methods, XRF is always detectable, requires no reporter probes (*i.e.* fluorophores), suffers minimal matrix effects, is sensitive to both bound and free metal ions and does not require vacuum conditions for almost all elements ($Z > 12$); this makes XRF an ideal tool for interrogating the biological metallome.

The use of synchrotron-based X-ray fluorescence imaging (XFI) to map the elemental composition of individual cells, tissues and organs can have a spatial resolution as low as tens of nanometres and is commonly used for studies of transition metals (Penner-Hahn, 2014; McRae *et al.*, 2009; Pushie *et al.*, 2014; Paunesku *et al.*, 2006; Punshon *et al.*, 2013; Ortega *et al.*, 2009; Vogt & Ralle, 2013; Zhao *et al.*, 2014; West *et al.*, 2014), and recently the use of XRF has been extended to include flow cytometry (Crawford *et al.*, 2016; Crawford & Penner-Hahn, 2018).

In synchrotron XRF, a sample is bombarded with a focused beam of photons with sufficient energy to excite core shell electrons, creating an electron–hole pair. Following ionization, outer-shell electrons relax to fill the core hole, resulting in the intrinsic emission of a photon (in the X-ray regime) with energy equivalent to the difference in energy between the two bound states. As such, the emission spectrum recorded by a solid-state energy-dispersive detector in an XRF (XFI if one is performing imaging) experiment (*e.g.* Fig. 1) comprises a series of peaks attributable to well defined X-ray emission lines and scatter together with a background signal. Even though X-ray emission lines are intrinsically Lorentzian in shape (Heckel & Scholz, 1987; Gunnink, 1977; Brunetti, 2013) with a full width at half-maximum (FWHM) of ∼10 eV, the experimental peak shape will be much broader as a result of Poisson statistics associated with electron–hole pair production when each photon strikes the detector, a function which is Gaussian with a FWHM of approximately 100 eV. The resulting peak is a Lorentzian–Gaussian convolution with a FWHM of ∼120 eV. Approaches to the processing and analysis of XRF data historically have used two main techniques to extract counts from the X-ray emission spectrum. A comparison between these two techniques is the subject of this paper.

1.1. Window binning

Integrative analysis, referred to herein as window binning (or just binning), is the simplest approach to XRF data analysis and is performed by summing all of the counts that are in an energy region of interest (ROI) corresponding to a specific elemental emission line. For example, this is represented in the inset in Fig. 1, where the Ca *Kα* (3.692 keV) emission is approximated as the total integrated counts striking the detector in the region between points ‘a’ and ‘b’. These integrated regions from each pixel of a sample can then be converted from fluorescence counts to elemental mass with reference to the corresponding integration for a standard, correcting each, if necessary, for the background counts. Window binning benefits from the fact that it is fairly straightforward and fast, only requires the single-channel analyzer values (SCAs, *i.e.* the integrated ROI sums) from data collection (just the reported integrated counts, not the full spectra), and is almost always performed directly at the

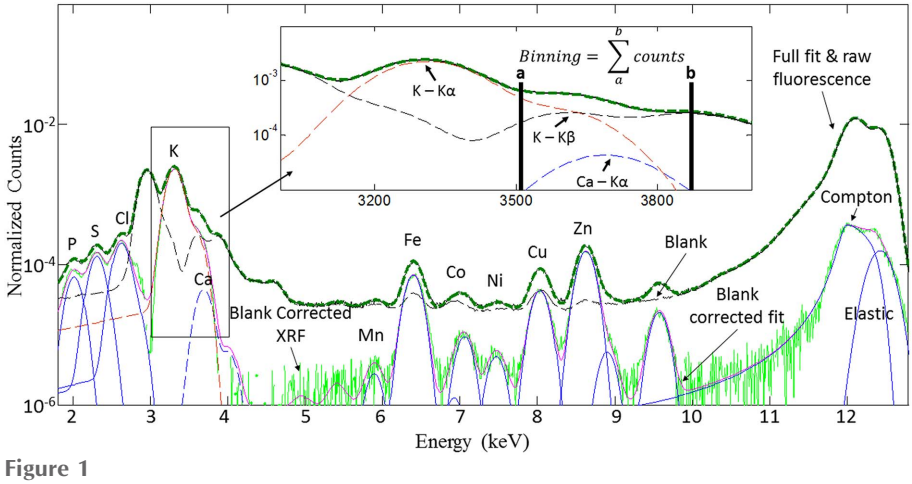

Figure 1
Fitted spectra sum of the full X-ray emission spectrum from mouse brain tissue presented in Fig. 3. The green, black, red and blue dashed lines correspond to the background, fit, and K and Ca *K* line emissions, respectively. The solid black, green and blue lines represents the raw X-ray fluorescence, blank (or background) corrected X-ray fluorescence and various other fitted emission lines, respectively. Inset: a close up of both the K and Ca *K* line emissions, showing both the fitted spectra as well as how window binning using the ROI from channel a to channel b would be applied for Ca *Kα* quantitation. The K *Kβ* and Ca *Kα* are in the same region of interest and thus the K emission will bleed into the Ca signal if the two signals are not properly deconvoluted.

beamline. In addition, it has not always been practical to process and save to disk the entire emission spectrum from each pixel with the image. However, as demonstrated below, this window-binning approach only works for the simplest samples because of peak overlap; the inset in Fig. 1 highlights the resulting peak overlap, in that the ROI for the Ca $K\alpha$ line also contains the K $K\beta$ and background fluorescence in a relative ratio of 1:20:20.

1.2. Fitting

Parametric analysis, referred to as fitting, is a more robust approach to the analysis in which the entire emission spectrum for each pixel is fit to a series of equations modeling the emission lines, background and scatter (Fig. 1). Doing so allows for complete deconvolution of overlapping lines (*e.g.* Ca $K\alpha$ and K $K\beta$, Cd *L*-lines and K *K*-lines). However, this approach takes longer, requires the full energy-resolved spectrum at each pixel and is more computationally demanding. A number of programs are available to deconvolute the emission spectrum in this way, including *MAPS* (Vogt, 2003), *PyMca* (Solé *et al.*, 2007), *AXIL* (Janssens *et al.*, 1996), *GeoPIXE* (Ryan *et al.*, 1995, 2010, 2014), *PyXRF* (Li *et al.*, 2017) and *M-BLANK* (Crawford, 2015, 2018).

1.3. Detector electronics

A comparison of these two approaches would be incomplete without also discussing changes at the level of data acquisition. The detector pre-amplifier pulse-train is typically fed to digital signal analyzer electronics (Pushie *et al.*, 2014) which quantifies the pulse heights, converting them to an energy spectrum such as that shown in Fig. 1. As described above, the processed peak is quite broad (Lorentzian–Gaussian convolution, FWHM > 100 eV) leading to spectral overlap of many emission lines (*e.g.* K $K\beta$ with Ca $K\alpha$). The widths of processed peaks contain contributions that are inherent to the detector and the pre-amplifier which represents an inherent resolution, but in addition to these there are also contributions (broadening) from the digital signal processing electronics. Newer digital signal processing electronics have more sophisticated and considerably faster pre-amplifier pulse-train handling, which can result in narrower peak shapes and therefore better spectral resolution.

Here we compare the results of binning and fitting analyses of XFI data. We also compare two major types of digital signal processing electronics, with the newer electronics showing a 30× increase in processing rate, leading to increased count rates, narrowing of the detector response function and decreased overlap of emission lines. To the best of our knowledge, except for the analysis methods reported by Alfeld & Janssens (2015), neither comparison has been formally presented. The comparisons are demonstrated using XFI data from post-photothrombotic stroke mouse brains, which contain a range of endogenous elements, with many overlapping fluorescence peaks distributed across a broad concentration range. This distribution is typical of almost all biological samples and tissues.

The goal of the present work is twofold. First, we highlight the errors associated when data are not completely deconvolved, and show that such errors are sample dependent and variable at the level of the pixel. Second, we show that incomplete deconvolution can lead to erroneous results, which, in the case presented, leads to an apparent reversal of observed trends of elemental distribution between anatomical regions.

2. Experimental

2.1. Sample preparation

Animal tissue used in this study was from an 11-week old male Balb/c photothrombotic stroke (PT) mouse model, following previously described methods (Winship & Murphy, 2008; Caine *et al.*, 2016; Hackett *et al.*, 2016). All experimental and surgical procedures were approved by the University of Saskatchewan's Animal Research Ethics Board, and followed the guidelines of the Canadian Council on Animal Care. Tissue was harvested following anaesthetization with 5% isofluorane and decapitation 72 h after the induction of the stroke. The head was frozen in liquid nitrogen immediately after decapitation to avoid artifacts arising from postmortem biochemical alterations (Hackett *et al.*, 2011, 2012, 2015). The brain was chiseled out from the frozen head in a −20°C chamber. Coronal sections of the brain, 30 µm thick, containing the central region of the infarct, were collected onto 'metal-free' plastic Thermanox coverslips, and allowed to air dry prior to XFI data collection.

2.2. XFI data collection

Elemental maps of brain sections were obtained using XFI performed at the Stanford Synchrotron Radiation Lightsource (SSRL) experimental stations 2-3, 10-2 and 14-3, as previously described (Caine *et al.*, 2016). We used an incident 12.5 keV X-ray beam with the beam size defined by either a 50 µm pinhole aperture (for 10-2) or a pair of KB-mirrors (for 2-3 and 14-3) (Kirkpatrick & Baez, 1948). The incident beam was at 45° to the sample mount; the sample was raster scanned through the beam with 30 µm steps and a beam exposure of 200 ms. X-ray fluorescence spectra were collected using a Vortex single-element silicon drift detector, positioned at 90° to the incident beam. Data were collected at 10-2 using DXP electronics, whereas the data from 2-3 and 14-3 were collected using Xspress 3 electronics at mean count rates of 10 kcounts s^{-1} and 630 kcounts s^{-1}, respectively. Reference foils of 6 µm thickness, containing known elemental areal concentrations, were measured for mass calibration purposes: P (GaP, 47.0 µg cm^{-2}); S (CuS, 95.1 µg cm^{-2}); K (KCl, 98.9 µg cm^{-2}); Ca (CaF_2, 56.8 µg cm^{-2}); Mn (Mn, 47.1 µg cm^{-2}); Fe (Fe, 56.0 µg cm^{-2}); Cu (CuS, 95.1 µg cm^{-2}); and Zn (ZnTe, 45.8 µg cm^{-2}) (Micromatter, Vancouver). At each pixel, the full XRF spectrum along with the SCA fluorescence lines for P, S, Cl, K, Ca, Mn, Fe, Cu, Zn and elastic scatter were recorded.

2.3. Digital signal processing electronics

Two major types of electronics designed for handling the pre-amplifier pulse-train are compared herein: DXP (X-ray Instrumentation Associates, Hayward CA, USA) and Xspress 3 (Quantum Detectors, Chilton Oxfordshire, UK). DXP electronics use a simple trapezoidal filtering of the pre-amplifier pulse-train to give an X-ray emission spectrum. Xspress 3 use a more sophisticated fitting process aided by considerably faster processors to quantify the pulse-train, with an increase of some 30× in processing speed over DXP (Xspress 3: Technical Datasheet, http://quantumdetectors.com/wp-content/uploads/2013/08/Xspress-3-Datasheet.pdf; Farrow *et al.*, 1995, 1998). This gives rise to increased maximum count rates and narrowing of the FWHM [data presented herein show a 30% decrease (96 eV *versus* 136 eV) at the K *Kα* energy, 3312.4 eV, for Xspress 3 relative to DXP] of peaks in the X-ray emission spectrum with a corresponding decrease in the overlap of features. We note in passing that although DXP electronics are very widespread indeed, that DXP and Xspress 3 represent different generations of digital-pulse processing electronics, and that both companies offer similar and competitive new technology such as the XIA FalconX and QD Xspress 3.

2.4. Binning of X-ray fluorescence

For binned analyses, the total integrated counts were converted to mass by comparison with the same binned fluorescence lines collected for a reference foil. As such, the binned values for each element were immediately analyzed without further refinement or processing using the program *SMAK* (Webb, 2011) written by Sam Webb at Stanford Synchrotron Radiation Lightsource.

2.5. Fitting of XFI data

Fitting analyses of XFI data were carried out using the data fitting program *M-BLANK* (Crawford, 2015, 2018). Briefly, and as described in more detail in the following sections, sample and non-sample pixels were identified automatically. The blank, or mean spectrum calculated from all non-sample pixels, was then subtracted from the spectrum of each pixel and the resulting spectra were then fit using linear least squares. This is identical to the blank spectrum being used as the background function during linear least squares fitting with its amplitude constrained to unity. In line with other XRF fitting programs, no data preparation of any kind was performed prior to fitting. Following fitting, each sample image was visually inspected to verify that appropriate sample and blank regions had been identified.

2.6. Conversion of fitted counts to mass

The same standard measurements used to convert binned counts to mass were also used to convert fitted counts to mass with the exception that the full energy spectrum was fitted for each standard and the total area under the curve for each element was used (rather than just a window of unfitted

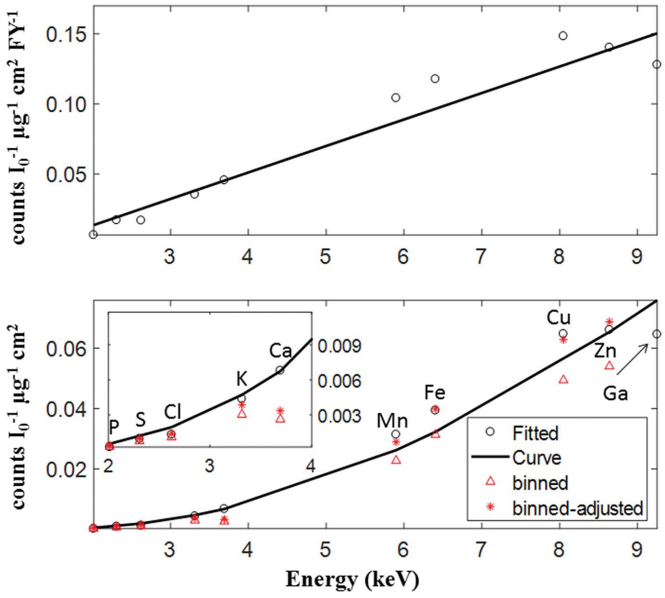

Figure 2
Mass calibrations for fitted datasets. (Top) The ratio of fitted counts normalized by incident-beam intensity divided by areal concentration and then normalized by theoretical fluorescence yield fit with a first-order polynomial. (Bottom) The fluorescence-normalized calibration curve from the first-order polynomial (from top) multiplied by the associated element's fluorescence yield to create the pseudo exponential calibration curve. The integrated (binned) normalized counts were overlaid. Because binning does not account for the entire area under a given element's fluorescence curve, the values are about ∼22% less than the values from fitting. Thus, the values were adjusted to yield the theoretical integrated counts at 100%. The inset is a close up of the 2 keV to 4 keV region.

counts). As shown in Fig. 2, the counts were divided by the fluorescence yield based on the excitation energy and then fit to a first-order polynomial. Although discussed elsewhere (Crawford, 2015; Crawford *et al.*, 2016; Crawford & Penner-Hahn, 2018), normalization by fluorescence yield significantly accounts for the exponential aspect of the calibration curve, with the result being fitted to a first-order polynomial because the correction is not perfect. The corresponding values for all elemental emissions were then interpolated or extrapolated from the fit. The resulting values were then multiplied by the corresponding fluorescence yield to give the theoretical response calibration of the detector in units of normalized counts per areal concentration. Importantly, unless corrected, attenuation of fluorescence by sample and standards makes areal concentrations semi-quantitative for elements $\sim Z < 20$. Such self absorption can be corrected for; however, since corrections were not applied for binning analyses, they were not applied for fitting analyses either.

2.7. Separation of sample and non-sample

Sample and non-sample pixels in each image were automatically separated in an iterative process using an ROI centered on the K *Kα* emission line (it had the greatest sample-to-background ratio in the brain sections employed) to generate a raw sample image (Crawford, 2015; Crawford *et al.*, 2016; Crawford & Penner-Hahn, 2018). Initially, all pixels with

intensities greater than 0.2× the maximum K signal were defined as 'sample'. Each iteration began by calculating the mean, $\bar{x}$, and standard deviation, σ, of the non-'sample' pixels. Any pixel with an intensity greater than $\bar{x} + 2\sigma$ was redefined as 'sample'. This process was repeated until the 'sample' population became self-consistent.

2.8. Calculation of fitting parameters

Fitting parameters (*i.e.* the energy calibration and the peak shapes) for the samples were derived from the samples themselves, not the standards. Sample scans were individually separated into sample and non-sample pixels and the mean spectrum for each region was calculated. The mean non-sample (background) spectrum, which is the blank, was used to correct the mean sample spectrum to yield the corrected spectrum, from which fitting parameters were calculated.

3. Results

3.1. DXP electronics

3.1.1. Insufficient deconvolution of overlapping emission peaks leads to incorrect elemental quantitation and localization. Fig. 3 shows representative Ca and K images from binned [Figs. 3(*a*) and 3(*b*), respectively] and fitted [Figs. 3(*d*) and 3(*e*), respectively] analyses of mouse brain tissue. The images from binned analyses for K and Ca are strikingly similar. In contrast, there is a stark difference between the binned and fitted images of Ca [Figs. 3(*b*) and 3(*e*), respectively]. In fact, the difference is such that the biological conclusions from each would be the opposite and therefore conflicting. Fig. 1 illustrates the origin of this difference, where the K $K\beta$ peak rests directly above the Ca $K\alpha$ peak. Thus, the windowed region for Ca cannot avoid the 'bleed through' of the K signal and therefore this artifact cannot be removed from analyses by binning alone.

Figs. 3(*c*) and 3(*f*) show overlays of Ca with K for binning and fitting analyses, respectively, confirming that these two approaches to data analysis yield strikingly different results. Although the fitted data (Fig. 3*f*) show an anticorrelation, in that K and Ca are prominent in different regions of the sample, the binned data (Fig. 3*c*) suggest the opposite, that Ca and K are correlated in their localization.

Fig. 3(*g*) shows the per-pixel correlation plot for binned Ca as a function of fitted Ca. In the ideal case, if there is no difference between binning and fitting, this would comprise a straight line with a slope of unity. Instead, the correlation plot shows significant deviation from this ideal, with most binned pixels significantly higher than the corresponding fitted pixels as a result of contributions from the K signal. The resulting plot (Fig. 3*g*) has been separated objectively into three different groups using expectation maximization (EM), a Gaussian mixture-based soft-clustering method (Ward *et al.*, 2013). Though similar to its use by Ward *et al.* (2013), EM was used to partition differently correlated regions between two analytical techniques; we have not used it to characterize the biological model. Assigning the colors from the plot to the corresponding pixel indices produces the brain image in Fig. 3(*h*). As can be seen, the different correlations obtained from binned analyses correspond to three distinct regions of

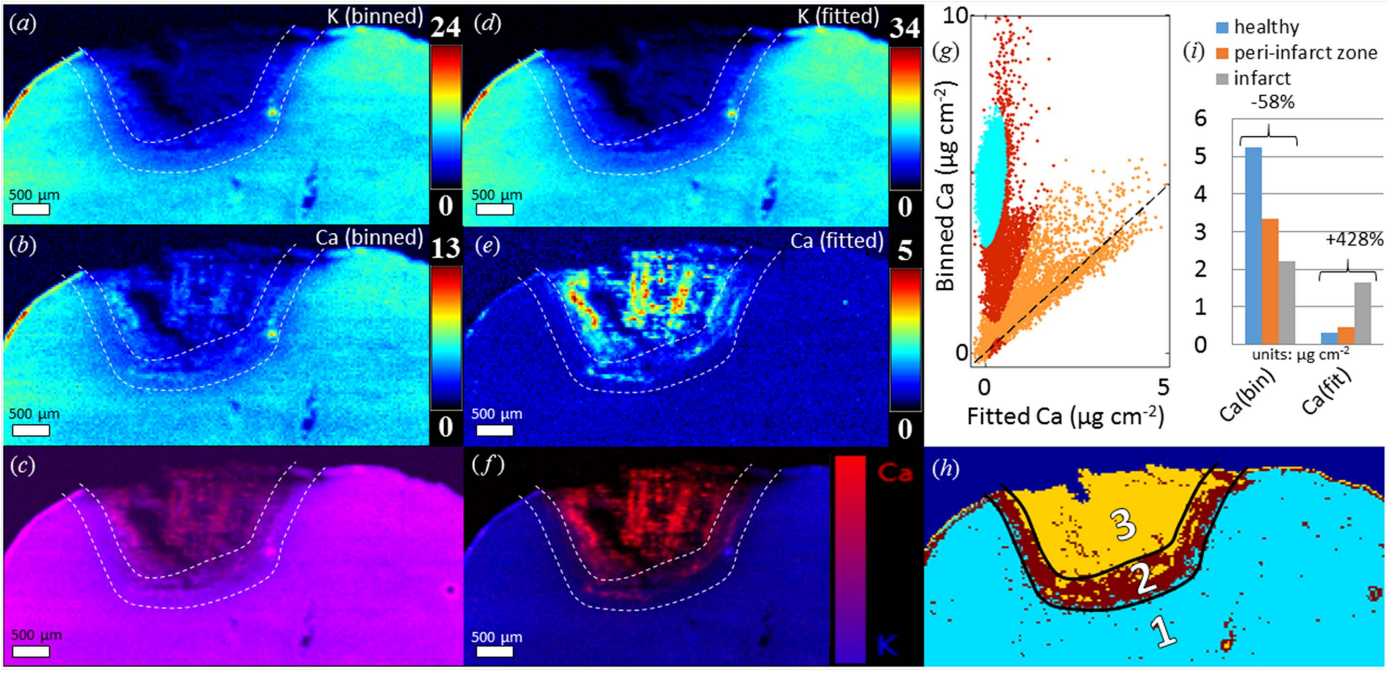

Figure 3
DXP binned and fitted analyses of Ca and K. Images produced by binned analyses for K (*a*) and Ca (*b*), and by fitted analyses for K (*d*) and Ca (*e*). Overlay images of Ca (red) and K (blue) from binned (*c*) and fitted (*f*) analyses. (*g*) The correlation plot of binned Ca as a function of fitted Ca with data regions separated using expectation maximization, a Gaussian mixture-based soft clustering method. (*h*) The reconstructed image from (*g*). (*i*) Bar plot of [Ca] in the three regions obtained from binning and fitting analyses, in units of µg cm^{-2}. Length scale bars are 500 µm.

the image [labeled in Fig. 3(*h*) as 1, 2 and 3] indicating different treatment of Ca fluorescence by binned analyses depending upon the spatial region of origin. The boundaries of these regions have been free-hand drawn and overlaid on Figs. 3(*a*)–3(*f*). Importantly, regions 1, 2 and 3, though not characteristically relevant, happen to coincide with regions of the photothrombotic model that are readily conceptualized within the current dogma of ischemic stroke theory (Caine *et al.*, 2016); healthy tissue, the peri-infarct zone and infarct, respectively. This should not necessarily be the case as clustering was performed on the correlation between the same element calculated by two different analytical techniques, not between different elements within a single analytical technique. Since these three separate regions mirror the three regions of the stroke model (Caine *et al.*, 2016), it makes it impossible to make reliable comparisons between these tissue regions for Ca (and for any other element where deconvolution is an issue) if binned analyses are used. Indeed, Fig. 3(*h*) demonstrates that quantification of Ca in the three regions shows not only a change in magnitude but a reversal of trend, comparing binning with fitting, in that Ca levels decrease between regions 1 to 3 for binning, but increase for fitting.

3.1.2. Insufficient deconvolution may lead to decreased precision. The results herein (considering the samples employed) suggest that binning can be less precise than fitting. Fig. 4 shows the histograms for the background pixels of the scan from Fig. 3 obtained from both binned and fitted analyses. For P, Cl, K and Ca, the distribution widths associated with the binned analyses are wider than those from the fitted analyses, indicating there may be an apparent increased signal noise caused by the decreased analytical precision associated with binned analyses. Ideally, the elemental content of the background should be fairly constant with an approximately Gaussian distribution (*S*) governed by the real elemental distribution (*R*), environmental noise (*N*), Poisson counting statistics (*C*) and analytical precision (*P*), such that $S = (R^2 + N^2 + C^2 + P^2)^{1/2}$. Since both the binning and fitting analyses of Fig. 4 processed identical data, *R*, *C* and *N* are identical and the only difference between the distributions obtained from the two analyses can be from analytical precision, *P*, which must be larger (poorer) for the binned data set.

It could be possible that the apparent difference in precision actually arises from differences in the mass calibrations between the two analyses. Binned analyses used the mass calibrations directly from the standards [Fig. 2 bottom, binned values, (*) with adjusted values, (Δ) for comparison with the fitted curve], whereas the fitted analyses used the best-fit curve to all the standards in order to achieve a better estimate of each standard's mass calibration (see above). If the mass calibration value (units of normalized counts per areal concentration) is larger for fitting relative to binning analyses, then this could potentially lead to the resulting observations shown. This is because a larger calibration value could result in a smaller absolute range in the spanned values for a given element. As can be seen from the calibration curve in Fig. 2 (bottom, inset), the adjusted binning calibration ratios for P, S, Cl, K and Ca are all smaller relative to the fitted calibration curve (black line). As such, although the decreased distribution widths (for fitting relative to binning) in Fig. 3 are to be expected (since we expect increased analytical precision from fitting relative to binning), this difference may completely or partly arise from the differences in mass calibrations and it is difficult to know exactly what portion arises from mass calibration differences and what portion arises from differences in analytical precision.

3.1.3. Trace elements register incremental amounts from binning analyses. The histograms for Mn shown in Fig. 4 show an issue that arises from low counting statistics. The detector registers an integer number of pulses proportional to the total number of photons that strike the detector area for a given energy. Normalization of the recorded fluorescence for a given element is then performed by dividing by the incident-beam intensity, which is recorded as a current between two charged plates inside an ion chamber immediately upstream from the sample (I_0). If the total amount of a given element is very low, such that the total detected fluorescence of the element registers a very low number of counts, then slight changes in the amount of that element may not be captured by the detector as a result of its discrete counting nature. The apparent subdivision into smaller peaks in the Mn histogram from binned data (Fig. 4) thus arises from the integer nature of counts. This is observed for

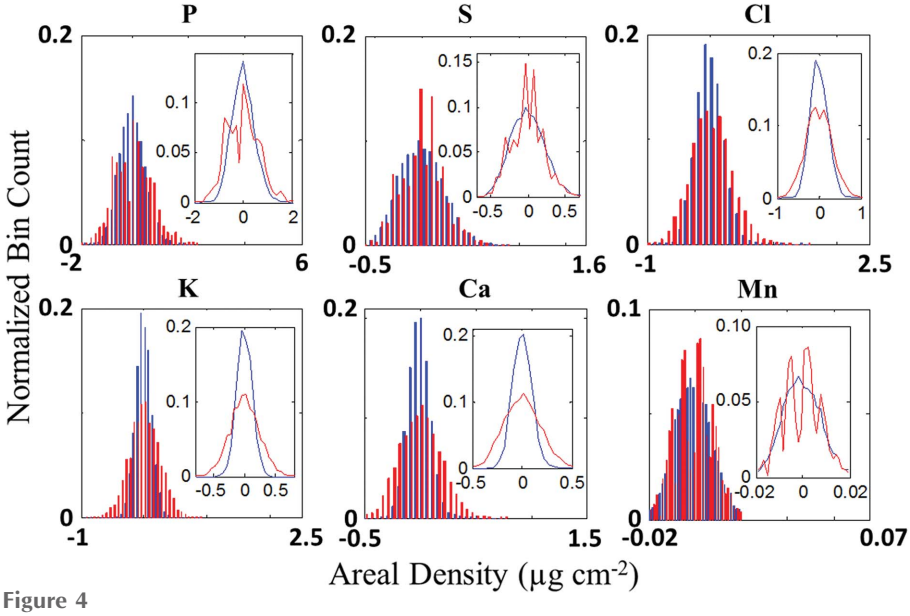

Figure 4
Background distributions: the histograms for the background pixels from the images in Fig. 3 showing binned (red) and fitted (blue) analyses for Mn, P, S, Cl, K and Ca. The inset in each plot shows the same data except the bars have been replaced by line plots.

Mn because it is present at ultra-trace levels and thus gives rise to very few counts at the detector. In the current example, the total number of detector counts (within the data collection dwell time) was around 10–20 from the entire integrated Mn *K*-line spectrum. Because of this, the histogram for the binned analyses appears in clumps and can be reconstructed by (what looks like) four individual Gaussian functions. The reason the values are Gaussian-clustered and not integer-clustered arises from fluctuations in I_0 and dead-time correction handled by the electronics. This is because dead-time correction leads to non-integer count readings; and for I_0, the readings, though integers, typically fluctuate or oscillate at a narrow range (typically ±1% during top-up mode) around very large numbers, and, although this fluctuation is not Gaussian, subsequent normalization of the dead-time corrected counts further leads to an apparent non-integer Gaussian-like distribution in counts.

3.2. Xspress 3 electronics

Xspress 3 electronics have a faster processing capability, which results in an observed 30% decrease in peak FWHM compared with DXP, based on the comparison of the K *Kα* detector response functions (FWHM: 136 eV and 96 eV for DXP and Xspress 3, respectively). The resulting spectra, however, appear to display the same artifacts as those noted for spectra from the DXP electronics, and, although these artifacts are less severe, the distortions from incomplete deconvolution of the K *Kβ* and Ca *Kα* peaks can still be seen. Fig. 5 demonstrates results from an adjacent section to the tissue in Fig. 3. By comparing the binned images [Figs. 5(*a*) and 5(*b*) for K and Ca, respectively] to the fitted images [Figs. 5(*c*) and 5(*d*) for K and Ca, respectively] it can be seen that the fitted image of Ca (Fig. 5*d*) shows much more contrast between the different regions than its binned counterpart (Fig. 5*b*). As can be seen from the correlation plot (Fig. 5*e*) of fitted Ca *versus* binned Ca and the resulting clustering image (Fig. 5*f*), two distinct regions still exist when the data are binned as opposed to fitted. The border of these two regions was used to define the end of the peri-infarct zone; the border between the peri-infarct and the infarct was drawn in manually along the morphological feature in the fitted K image (Fig. 5*c*) indicated by the arrows. Although the trend in localization is no longer reversed [as it was from the DXP analyses, Fig. 3(*h*)], a comparison of the areal concentrations from binned and fitted analyses (Fig. 5*g*) shows that the shift in concentrations is still significant and very much distorted when the data are binned.

Because the artifact arises from the overlap of the K *Kβ* with the Ca *Kα*, one might assume that the central infarct region of the tissue (region 1) may be free of the artifact, since K is extremely low in this region; this would appear to be in

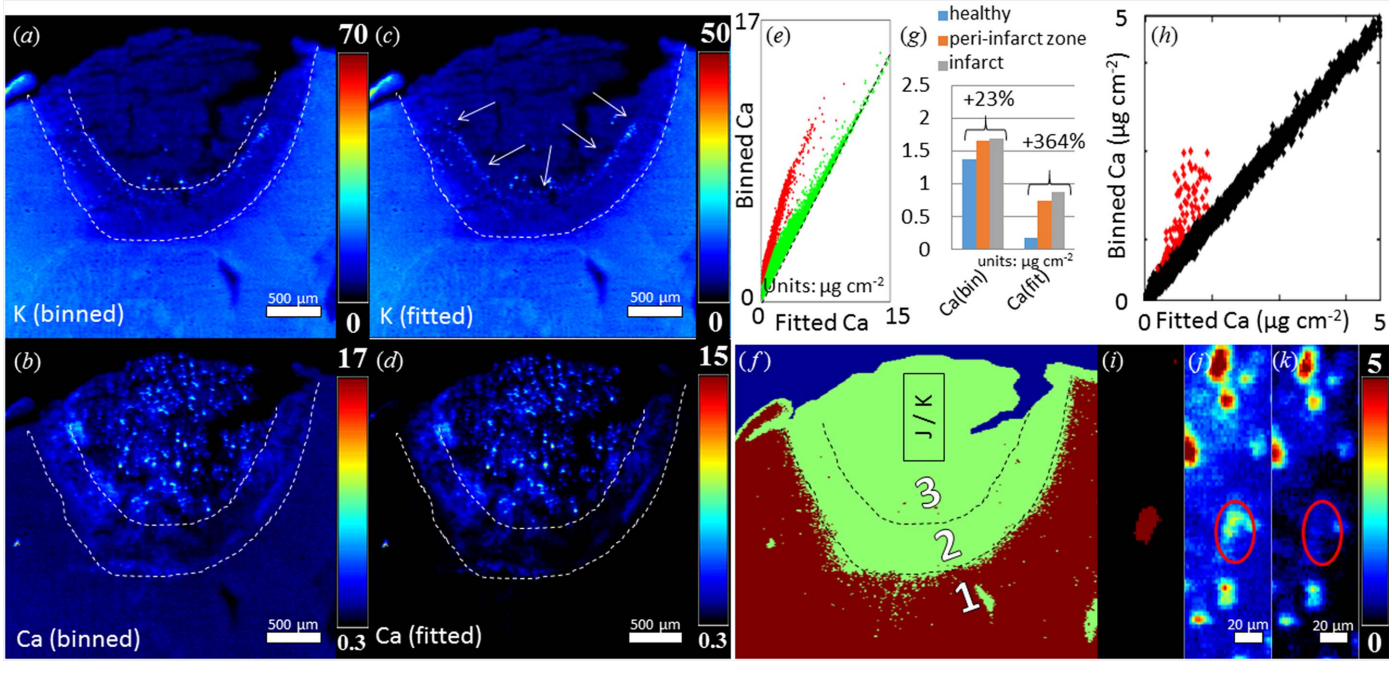

Figure 5
Xspress 3 data analyses and comparisons: (*a*)–(*g*) are from an adjacent section to that of Fig. 3 and were collected at BL 14-3; (*h*)–(*k*) are based on a high-resolution image of that same section collected at BL 2-3. (*a*) and (*b*) Binned K and Ca images along with their fitted counterparts (*c*) and (*d*) from an adjacent section to the image in Fig. 3. (*e*) and (*f*) The per-pixel correlations of binned Ca as a function of fitted Ca; the dashed black line indicates a ratio of 1:1. The partitioned regions have been restructured into the image in (*f*). A third region was partitioned by using the morphological structure in (*c*), demarcated by the arrows, as the outline for a second boundary. These regions have been labeled 1, 2 and 3 and are overlaid on (*a*)–(*d*) to represent the healthy tissue, peri-infarct zone and infarct, respectively. (*g*) A bar plot showing the apparent [Ca] in healthy tissue, peri-infarct zone and infarct from binned and fitted analyses for the tissue sections represented by (*f*). (*j*) and (*k*) A close up high-resolution scan of Ca within the infarct (rectangle region in *f*) analyzed using binning (*j*) and fitting (*k*). (*h*) Correlation plot of fitted *versus* binned Ca from (*j*) and (*k*). (*i*) Reconstructed image from the separated cluster from (*h*). Scale bars: (*a*)–(*d*), 500 µm; (*j*) and (*k*), 20 µm. Intensity bars are in units of µg cm^{-2}.

agreement with Fig. 5(*e*) (the green values have a slope of one and intercept of zero). However, such an assumption is wrong. Binned (Fig. 5*j*) and fitted (Fig. 5*k*) Ca images were produced from an additional scan conducted within the region identified in Fig. 5(*f*). These two images are different. As can be seen in the cluster image (Fig. 5*i*) constructed from the two different groupings from the correlation plot (Fig. 5*h*) of fitted Ca *versus* binned Ca, a subregion exists inside the image where the K $K\beta$ peak is bleeding through into the Ca $K\alpha$ window. This region is circled in Figs. 5(*j*) and 5(*k*) and, as can be seen in Fig. 5(*j*), the apparent hotspot of Ca is almost entirely absent when the data are fitted (Fig. 5*k*).

4. Discussion

The strong similarity of Ca to K in the binned dataset (Figs. 3*a* and 3*b*) arises from the inability to deconvolute the relatively large contribution arising from the K $K\beta$-line from the Ca $K\alpha$-line. This results in the strong K signal dominating the apparent Ca signal (Fig. 1 inset) in all locations where there is K. The only potentially valid Ca signal from the binned dataset is within the infarct; and even there the apparent signal is much weaker than the binned Ca signal outside the infarct. This overlap of K $K\beta$ with Ca $K\alpha$ explains the unexpected Ca results found by Caine *et al.* (2016), which we note the authors had correctly surmised.

Qualitatively, image comparisons for any element besides Ca look more or less the same between binned and fitted datasets. However, though not shown here, all elements displayed differential quantitation between the two analytical techniques across the model regions. The comparison, shown here of binned and fitted Ca, shows three sub-populations of differential quantitation between the two techniques for data obtained from the DXP electronics. This differential quantitation between binning and fitting is very important in the chosen example dataset, since the three subpopulations demarcate conceptually relevant regions within the stroke model, namely the infarct, the surrounding peri-infarct zone and healthy tissue. The presence of these subpopulations means that the apparent value from binning is dependent on what else is there in the pixel and this means that binning is susceptible to 'matrix' effects. Importantly, this means that quantitative comparisons from the three different regions cannot be made, *i.e.* the Ca levels in the infarct cannot be properly compared with the Ca from either of the other two regions when binning is employed.

In terms of mass calibration, we only normalized by fluorescent yield, which is expected to give a reasonable calibration. We recognize that additional normalization to the photoelectric cross section would be of more interest and also the quantum efficiency of the detector could be taken into account, allowing for a much more meaningful sensitivity curve. We note that this could explain especially the reduced sensitivity for Ga, as a greater part of its radiation passes through the detector undetected. Accounting for this may have adjusted the fitted sensitivities slightly; however, the difference between measured and fitted sensitivity for both K and Ca is negligible (Fig. 2).

Although the use of new Xspress 3 electronics leads to narrower peak shapes with decreased overlap of elemental emissions, the problems persist. While the three subpopulations present in Fig. 3 have been reduced to two in Fig. 5, these subpopulations still separate the peri-infarct/infarct region from the healthy tissue showing that these two regions cannot be compared. Also, although the trend of Ca localization reflects the fitted observation (the change is in the same direction), the magnitude of that trend is significantly decreased for the binned data, indicating that binned analyses are less sensitive.

Although it might be expected that the impact of K on Ca might be absent in the infarct since the K is almost completely absent in that region, convolution artifacts still exist in the Ca signal from the K signal in the infarct (where the K signal is weakest) as can be seen in Figs. 5(*h*)–5(*k*).

Collectively, the results from Figs. 3 and 5 demonstrate that (even with faster electronics) the inability of binned analyses to deconvolute overlapping peaks affects the entire dataset, and that it affects the data differently across the dataset.

Incomplete peak deconvolution of window-binned data can lead to erroneous data interpretations not only between Ca $K\alpha$ and K $K\beta$, but for any other elements when emission lines are close in energy such as Hg $L\alpha_1$ and Zn $K\beta$. As such, for most biological samples quantitative analyses may only be reliable if full peak-shape deconvolution is performed. Unfortunately, some emissions (such as the Cd *L*-lines and K *K*-lines) can never be resolved with conventional solid-state detectors irrespective of any enhancements to detector resolution, because they are quite simply too close to one another and almost exactly overlap.

In addition to binned analyses having a loss in accuracy for elements with overlapping emission lines, Fig. 4 demonstrates that decreased precision can be seen in the larger distribution widths, and that an additional loss in accuracy can be seen as binned analyses report incremental amounts for ultra-trace elements attributed to the integer nature of photon counting. Where fitting is able to solve for fractional counts, binned analyses cannot.

5. Conclusions

Fitting gives superior estimation of quantities whereas binning can result in artifacts. This conclusion is regardless of the detector electronics used during data acquisition or the fitting program employed (we expect any of the aforementioned programs to yield similar results). The potential implications of artifacts and the consequential erroneous conclusions that might arise will be sample specific, and will not be constant across samples.

The artifacts present in analyses based solely on binned data can impact both apparent localization and apparent quantitation. Even with the advent of faster detector electronics with improved electron pulse-train handling, the inability to deconvolute overlapping peaks still presents

errors. Although the presence or impact of bleed-through artifacts was attenuated with the use of new electronics, errors still arose from binned analyses alone.

The data herein compared XRF data collected using Xspress 3 and DXP electronics which had energy resolutions of 96 eV and 136 eV at the K $K\alpha$ energy, 3312.4 eV, respectively; and the bleed-through artifacts from overlapping emission lines were attenuated for Xpress 3 relative to DXP. However, XRF experiments using synchrotron facilities are sometimes performed with an energy resolution far above 200 eV to allow for higher count rates. In such cases, the differences between fitting and binning will become even more pronounced.

Ultimately, this work demonstrates that the best practice is to use properly fitted data and not to rely on binned analyses if the full XRF spectra are available. In the case that full spectra are not available, analyses using binned data should be considered to provide only skeptical semi-quantitative elemental distributions.

Acknowledgements

The authors would also like to acknowledge the contribution of Sharleen Weese Maley for her expert administrative and technical assistance and assistance in editing the manuscript.

Funding information

This research was supported by a Saskatchewan Health Research Foundation Establishment Grant to MEK. Funding for this project is also provided by the Heart & Stroke Foundation and SHRF along with the University of Saskatchewan for the Saskatchewan Research Chair in Clinical Stroke Research (MEK), as well as a joint Canadian Institutes of Health Research (CIHR)/Heart & Stroke Foundation Synchrotron Medical Imaging Team (Grant No. CIF 99472 to HKN, MEK, GNG, IJP and others). AMC is a Fellow in the CIHR Training grant in Health Research Using Synchrotron Techniques (CIHR-THRUST, IJP and others). GNG and IJP are Canada Research Chairs. Research in the George and Pickering groups is supported by NSERC Discovery Grants (to GNG and IJP), and by the Government of Saskatchewan Innovation and Science Fund (IJP). Portions of this research were carried out at the Stanford Synchrotron Radiation Lightsource, a Directorate of SLAC National Accelerator Laboratory and an Office of Science User Facility operated for the US Department of Energy Office of Science by Stanford University. The SSRL Structural Molecular Biology Program is supported by the DOE Office of Biological and Environmental Research, and by the National Institutes of Health, National Center for Research Resources, Biomedical Technology Program (P41RR001209).

References

Alfeld, M. & Janssens, K. (2015). *J. Anal. At. Spectrom.* **30**, 777–789.
Brunetti, A. (2013). *Comput. Phys. Commun.* **184**, 573–578.
Caine, S., Hackett, M. J., Hou, H., Kumar, S., Maley, J., Ivanishvili, Z., Suen, B., Szmigielski, A., Jiang, Z., Sylvain, N. J., Nichol, H. & Kelly, M. E. (2016). *Neurobiol. Dis.* **91**, 132–142.
Crawford, A. M. (2015). PhD thesis, University of Michigan, USA.
Crawford, A. M., Deb, A. & Penner-Hahn, J. E. (2018). *M-BLANK: a program for fitting of X-ray fluorescence spectra.* Submitted.
Crawford, A. M., Kurecka, P., Yim, T. K., Kozemchak, C., Deb, A., Dostál, L., Sun, C.-J., Brewe, D. L., Barrea, R. & Penner-Hahn, J. E. (2016). *J. Synchrotron Rad.* **23**, 901–908.
Crawford, A. M. & Penner-Hahn, J. E. (2018). *Cellular Heterogeneity: Methods and Protocols*, 1st ed., edited by N. S. Barteneva & I. A. Vorobjev. New York: Humana Press.
Farrow, R., Derbyshire, G. E., Dobson, B. R., Dent, A. J., Bogg, D., Headspith, J., Lawton, R., Martini, M. & Buxton, K. (1995). *Nucl. Instrum. Methods Phys. Res. B*, **97**, 567–571.
Farrow, R. C., Headspith, J. H., Dent, A. J., Dobson, B. R., Bilsborrow, R. L., Ramsdale, C. A., Stephenson, P. C., Brierley, S., Derbyshire, G. E., Sangsingkeow, P. & Buxton, K. (1998). *J. Synchrotron Rad.* **5**, 845–847.
Fierke, C. A. & Thompson, R. B. (2001). *Biometals*, **14**, 205–222.
Groombridge, A. S., Miyashita, S., Fujii, S., Nagasawa, K., Okahashi, T., Ohata, M., Umemura, T., Takatsu, A., Inagaki, K. & Chiba, K. (2013). *Anal. Sci.* **29**, 597–603.
Gunnink, R. (1977). *Nucl. Instrum. Methods*, **143**, 145–149.
Hackett, M. J., Britz, C. J., Paterson, P. G., Nichol, H., Pickering, I. J. & George, G. N. (2015). *ACS Chem. Neurosci.* **6**, 226–238.
Hackett, M., McQuillan, J., El-Assaad, F., Aitken, J. B., Levina, A., Cohen, D. D., Siegele, R., Carter, E. A., Grau, G. E., Hunt, N. & Lay, P. A. (2011). *Analyst*, **136**, 2941–2952.
Hackett, M. J., Smith, S. E., Paterson, P. G., Nichol, H., Pickering, I. J. & George, G. N. (2012). *ACS Chem. Neurosci.* **3**, 178–185.
Hackett, M. J., Sylvain, N. J., Hou, H., Caine, S., Alaverdashvili, M., Pushie, M. J. & Kelly, M. E. (2016). *Anal. Chem.* **88**, 10949–10956.
Heckel, J. & Scholz, W. (1987). *X-ray Spectrom.* **16**, 181–185.
Herring, W. B., Leavell, B. S., Paixao, L. M. & Yoe, J. H. (1960*a*). *Am. J. Clin. Nutr.* **8**, 846–854.
Herring, W. B., Leavell, B. S., Paixao, L. M. & Yoe, J. H. (1960*b*). *Am. J. Clin. Nutr.* **8**, 855–863.
Ho, K.-S. & Chan, W.-T. (2010). *J. Anal. At. Spectrom.* **25**, 1114–1122.
Janssens, K., Vekemans, B., Adams, F., van Espen, P. & Mutsaers, P. (1996). *Nucl. Instrum. Methods Phys. Res. B*, **109–110**, 179–185.
Kakkar, N. & Makkar, M. (2009). *Lab. Med.* **40**, 549–555.
Kikuchi, K., Komatsu, K. & Nagano, T. (2004). *Curr. Opin. Chem. Biol.* **8**, 182–191.
Kirkpatrick, P. & Baez, A. V. (1948). *J. Opt. Soc. Am.* **38**, 766–774.
Li, L., Yan, H., Xu, W., Yu, D., Heroux, A., Lee, W., Campbell, S. I. & Chu, Y. S. (2017). *Proc. SPIE*, **10389**, 103890U.
McRae, R., Bagchi, P., Sumalekshmy, S. & Fahrni, C. J. (2009). *Chem. Rev.* **109**, 4780–4827.
Miyashita, S., Groombridge, A. S., Fujii, S., Minoda, A., Takatsu, A., Hioki, A., Chiba, K. & Inagaki, K. (2014). *J. Anal. At. Spectrom.* **29**, 1598–1606.
Mueller, L., Traub, H., Jakubowski, N., Drescher, D., Baranov, V. I. & Kneipp, J. (2014). *Anal. Bioanal. Chem.* **406**, 6963–6977.
Ortega, R., Deves, G. & Carmona, A. (2009). *J. R. Soc. Interface*, **6**, S649–S658.
Paunesku, T., Vogt, S., Maser, J., Lai, B. & Woloschak, G. (2006). *J. Cell. Biochem.* **99**, 1489–1502.
Penner-Hahn, J. E. (2014). *Metallomics and the Cell*, edited by L. Banci. Dordrecht: Springer.
Punshon, T., Ricachenevsky, F. K., Hindt, M. N., Socha, A. L. & Zuber, H. (2013). *Metallomics*, **5**, 1133–1145.
Pushie, M. J., Pickering, I. J., Korbas, M., Hackett, M. J. & George, G. N. (2014). *Chem. Rev.* **114**, 8499–8541.
Ryan, C. G., Jamieson, D. N., Churms, C. L. & Pilcher, J. V. (1995). *Nucl. Instrum. Methods Phys. Res. B*, **104**, 157–165.
Ryan, C. G., Kirkham, R., Hough, R. M., Moorhead, G., Siddons, D. P., de Jonge, M. D., Paterson, D. J., De Geronimo, G., Howard,

D. L. & Cleverley, J. S. (2010). *Nucl. Instrum. Methods Phys. Res. A*, **619**, 37–43.
Ryan, C. G., Siddons, D. P., Kirkham, R., Li, Z. Y., de Jonge, M. D., Paterson, D. J., Kuczewski, A., Howard, D. L., Dunn, P. A., Falkenberg, G., Boesenberg, U., De Geronimo, G., Fisher, L. A., Halfpenny, A., Lintern, M. J., Lombi, E., Dyl, K. A., Jensen, M., Moorhead, G. F., Cleverley, J. S., Hough, R. M., Godel, B., Barnes, S. J., James, S. A., Spiers, K. M., Alfeld, M., Wellenreuther, G., Vukmanovic, Z. & Borg, S. (2014). *J. Phys. Conf. Ser.* **499**, 012002.
Shamberger, R. J. (2003). *Biol. Trace Elem. Res.* **94**, 123–129.
Solé, V. A., Papillon, E., Cotte, M., Walter, P. & Susini, J. (2007). *At. Spectrosc.* **62**, 63–68.
Vogt, S. (2003). *J. Phys. IV Fr.* **104**, 635–638.
Vogt, S. & Ralle, M. (2013). *Anal. Bioanal. Chem.* **405**, 1809–1820.
Wang, D., Hosteen, O. & Fierke, C. A. (2012). *J. Inorg. Biochem.* **111**, 173–181.
Ward, J., Marvin, R., O'Halloran, T., Jacobsen, C. & Vogt, S. (2013). *Microsc. Microanal.* **19**, 1281–1289.
Webb, S. M. (2011). *AIP Conf. Proc.* **1365**, 196–199.
West, M., Ellis, A. T., Potts, P. J., Streli, C., Vanhoof, C. & Wobrauschek, P. (2014). *J. Anal. At. Spectrom.* **29**, 1516–1563.
Winship, I. R. & Murphy, T. H. (2008). *J. Neurosci.* **28**, 6592–6606.
Yang, L. C., McRae, R., Henary, M. M., Patel, R., Lai, B., Vogt, S. & Fahrni, C. J. (2005). *Proc. Natl Acad. Sci.* **102**, 11179–11184.
Zhao, F. J., Moore, K. L., Lombi, E. & Zhu, Y. G. (2014). *Trends Plant Sci.* **19**, 183–192.